

Journal of Materials Chemistry A

Accepted Manuscript



This is an *Accepted Manuscript*, which has been through the Royal Society of Chemistry peer review process and has been accepted for publication.

Accepted Manuscripts are published online shortly after acceptance, before technical editing, formatting and proof reading. Using this free service, authors can make their results available to the community, in citable form, before we publish the edited article. We will replace this *Accepted Manuscript* with the edited and formatted *Advance Article* as soon as it is available.

You can find more information about *Accepted Manuscripts* in the [Information for Authors](#).

Please note that technical editing may introduce minor changes to the text and/or graphics, which may alter content. The journal's standard [Terms & Conditions](#) and the [Ethical guidelines](#) still apply. In no event shall the Royal Society of Chemistry be held responsible for any errors or omissions in this *Accepted Manuscript* or any consequences arising from the use of any information it contains.



Journal Name

ARTICLE

Constructing the Optimal Conductive Network in MnO-Based Nano Hybrids as High-Rate and Long-Life Anode Materials for Lithium-Ion Batteries

Received 00th January 20xx,
Accepted 00th January 20xx

DOI: 10.1039/x0xx00000x

www.rsc.org/

Dai-Huo Liu,[†] Hong-Yan Lü,[†] Xing-Long Wu,^{*†} Bao-Hua Hou,[†] Fang Wan,[†] Sheng-Da Bao,[†] Qingyu Yan,^{*‡,||} Hai-Ming Xie[†] and Rong-Shun Wang^{*†}

Among the transition metal oxides as anode for lithium ion batteries (LIBs), MnO material should be the most promising one due to its many merits mainly relatively low voltage hysteresis. However, it still suffers from inferior rate capabilities and poor cycle life arising from kinetic limitations, drastic volume changes and severe agglomeration of active MnO particulates during cycling. In this paper, by integrating the typical strategies of improving the electrochemical properties of transition metal oxides, we had rationally designed and successfully prepared one superior MnO based nano hybrid (MnO@C/RGO), in which carbon-coated MnO nanoparticles (MnO@C NPs) were electrically connected by the three-dimensional conductive networks composed of flexible graphene nanosheets. Electrochemical tests demonstrated that, the MnO@C/RGO nano hybrid not only showed the best Li storage performance in comparison with the commercial MnO material, MnO@C NPs and carbon nanotubes enhanced MnO@C NPs, but also exhibited much improved electrochemical properties compared with most of the previously reported MnO-based materials. The superior electrochemical properties of the MnO@C/RGO nano hybrid included high specific capacity (up to 847 mAh g⁻¹ at 80 mA g⁻¹), excellent high-rate capabilities (for example, delivering 451 mAh g⁻¹ at a very high current density of 7.6 A g⁻¹) and long cycle life (800 cycles without capacity decay). More importantly, we had for the first time achieved the charging/discharging of MnO-based materials without capacity increase even after 500 cycles by adjusting the voltage range, making the MnO@C/RGO nano hybrid more possible to be really practical anode material for LIBs.

Introduction

Recently, the fields of portable electronic devices, large-scale energy-storage stations and (hybrid) electric vehicles are seeking rapid development, which puts forward increasingly higher requirements for lithium ion batteries (LIBs), including higher energy/power densities and longer cycle life.¹⁻³ In order to meet these ever-increasing demands well, researches have focused on the much enhanced electrode materials, because the performances of LIBs intimately depend on the electrochemical properties of the constituents especially the electrode materials.⁴ The crucial evaluation parameters for the LIBs' electrode materials mainly include specific capacity, rate capabilities and cycling performance, in which the former two are almost decisive to the energy and power densities of LIBs respectively and the latter one incorporated with electrolyte and assembly processes would finally determine

the cycle life of LIBs.⁵⁻⁷ Therefore, developing the electrode materials with high specific capacity, superior rate capabilities and cycling performance are significantly crucial for building the next-generation advanced LIBs.

In the available electrode materials for LIBs, the selectable and practical anode materials are very limited in comparison with the cathode ones. Presently, the commonly used anode materials in the commercial LIBs are just pure or silicon/tin-containing carbonaceous materials,⁸ in which the former occupies the market share of over 95%. Thus, it is of importance and urgency to develop more alternative anode materials with superior properties, which has been pursued over the past ten to twenty years.⁹⁻¹¹ Among the anode materials proposed, transition metal oxides (TMOs) should be one of the most important candidates, which has been intensively studied because of their higher theoretical specific capacity of usually >700 mA h g⁻¹ than that of 372 mA h g⁻¹ of graphite. The commonly studied TMOs as anode materials for LIBs include Fe₂O₃,¹²⁻¹⁵ Fe₃O₄,¹⁶⁻¹⁹ Co₃O₄,²⁰⁻²² MnO,²³⁻³⁷ SnO₂,³⁸⁻⁴¹ NiO,⁴² CuO⁴³ and MoO₃,⁴⁴ in which MnO may be the most promising one due to its relatively lower voltage hysteresis (<0.8 V) compared to other TMOs, suitable reversible potential (~1.0V vs. Li⁺/Li), high density (5.43 g cm⁻³), as well as the high theoretical capacity of 756 mA h g⁻¹, relatively low cost and environmental benignity.²⁸⁻³⁰ Nevertheless, the intrinsically low conductivity of MnO material

[†] National & Local United Engineering Laboratory for Power Batteries, and Faculty of Chemistry, Northeast Normal University, Changchun 130024, China. Email addresses: xinglong@nenu.edu.cn (X. W.); wangrs@nenu.edu.cn (R. W.)

[‡] School of Materials Science and Engineering, Nanyang Technological University, 50 Nanyang Avenue, Singapore 639798, Singapore Email addresses: alexyan@ntu.edu.sg (Q. Y.).

^{||} Energy Research Institute@NTU, Nanyang Technological University, Singapore 637459, Singapore.

makes it suffer from inferior rate capacity and poor cycling stability arising from kinetic limitations, the rapid capacity fading resulting from severe agglomeration and drastic volume changes during the lithiation/delithiation processes, as other TMOs confronted. Furthermore, the repeating volume changes during cycling could also give rise to the pulverization of the entire MnO electrodes, and hence the Mn shedding and dissolution into the electrolyte.³⁷

In previous studies, tremendous efforts have been made to tackle the above-mentioned issues with the expectance of significantly increasing the electrochemical properties of MnO based materials when used as anode for LIBs. The most effective approaches include: 1) preparing the nanometer-sized MnO particulates to shorten the diffusion lengths of both electrons and lithium ions;²⁷ 2) coating MnO particles with electrochemically stable and highly conductive materials, mainly carbonaceous materials, to stabilize the interfaces and enhance the rate capabilities;^{24, 25, 45} 3) constructing novel nanostructures in the composites by using conductive and flexible carbonaceous materials of two-dimensional (2D) graphene or one-dimensional (1D) carbon nanotubes to optimize the conductive networks and accommodate the volume changes during cycling.^{31-34, 46} Although each of the above three methods is efficient in enhancing the electrochemical properties of MnO materials as anode for LIBs, the level of improvement is still limited. Hence, developing new strategies to further improve the electrochemical properties will be highly meaningful to construct advanced MnO-based anode materials, which may be able to further improve its electrochemical performances and finally make MnO-based materials meet the LIBs' ever-increasing demands of high energy/power densities and long cycle life.

In addition to the problems of low conductivity, severe agglomeration and drastic volume changes when used as anode for LIBs, another drawback of the MnO-based materials as well as many other oxides is that, the delivered capacities are progressively increasing along with cycling. Although this phenomenon is a commonplace as described in many previously reported papers^{23-27, 47, 48}, the gradually increased capacities not only are actually superfluous for practical application but also implies the existence of some side electrochemical reactions, which might act as the inducement of instability in the following cycles. Unfortunately, there has still been no effective method reported to effectively solve this problem as far as we know.

Herein, by controlling the size of MnO particles and optimizing the conductive networks composed of two different carbon materials, we rationally design a high-performance MnO-based nanohybrid (MnO@C/RGO), in which carbon-coated MnO nanoparticles (MnO@C NPs) in the diameters of 80-120 nm embed into the three-dimensional (3D) conductive networks which are constructed by the flexible 2D reduced graphene oxide (RGO) nanosheets. Because the present MnO@C/RGO nanohybrid integrates all of the above-mentioned three characteristics, the electrochemical tests demonstrate that it exhibits as expected the best lithium storage properties in terms of the highest specific capacity and the most outstanding rate and cycling performances in

comparison with the commercial MnO products (C-MnO), ordinary carbon-coated MnO@C nanomaterials and even MnO@C/CNTs nanocomposites (MnO@C NPs electronically connected by 1D carbon nanotubes). Moreover, we have for the first time suppressed the progressively increased capacity upon cycling by adjusting the voltage range after ascertaining the reasons, making the MnO-based material more possibility to be used as actually practical anode materials for LIBs.

Experimental Section

Chemicals

All the chemicals of MnCl₂·4H₂O (>99.0%), MnO (>99.5%), sodium oleate (>99.5%), n-hexane (>99.0%), carbon nanotubes (>98.0%) and ethanol (99.7%) are of analytical grade (Sigma-Aldrich) and were used as received without further purification.

Preparation of reduced graphene oxide (RGO)

Graphene oxide (GO) was firstly prepared from natural graphite powder via a modified Hummers method.⁴⁹ An alcoholic exfoliated GO suspension (100 mL, approximately 500 mg) was obtained by dispersing the resultant GO product in ethanol under ultrasonication for above 6 hours. After removing the ethanol from the suspension by rotary evaporation under vacuum at 60 °C, the RGO nanosheets could be obtained by annealing the GO products at 1000 °C (heating rate: 20 °C min⁻¹) in an atmosphere of 5 vol% H₂ in N₂ for 2 h.

Synthesis of the MnO-based nanocomposites

Firstly, The manganese oleate precursor was prepared by a simple chemical reaction of MnCl₂ and sodium oleate.⁵⁰ In a typical process, 0.49 g of MnCl₂·4H₂O (~2.5 mmol) and 1.52 g of sodium oleate (~5 mmol) were dissolved in a mixture of ethanol (14 mL), H₂O (8 mL) and n-Hexane (50mL) with continuous stirring at room temperature for 4 h. The color of the upper of the mixture gradually changed to light brown. The upper Mn(oleate)₂/n-hexane solution (organic phase) could be collected after washing with 50 ml deionized water for five times. For preparing the MnO@C/CNTs and MnO@C/RGO nanohybrids, CNTs and RGO should be further added into the Mn(oleate)₂/n-hexane solution with continuous stirring at room temperature respectively. And then, the solvents were removed from the obtained mixture solutions by rotary evaporation under vacuum at 60 °C, resulting in the formation of raw materials for the preparation of the MnO@C NPs, MnO@C/CNTs and MnO@C/RGO nanohybrids. Finally, the expected MnO-based materials could be obtained by annealing the corresponding raw materials at 750 °C (heating rate: 1 °C min⁻¹) in the N₂ atmosphere for 2 h.

Structural characterizations

X-ray powder diffraction (XRD) were carried out using a Bruker D8 ADVANCE diffractometer with filtered Cu K α radiation (λ = 1.5406 Å). Raman spectra were measured on a Renishaw Invia

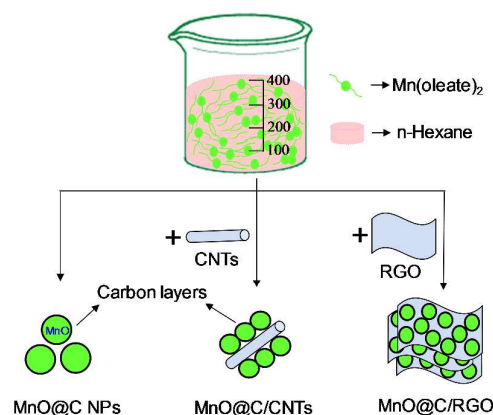


Figure 1. Schematic illustration of the preparation procedures and microstructures of MnO@C NPs, MnO@C/CNTs and MnO@C/RGO nanohybrids.

spectrometer using an Ar⁺ laser of 514.5 nm at room temperature. XPS measurements were implemented using a VG MultiLab 2000 system with a monochromatic Al K α X-ray source (Thermo VG Scientific). The morphology and microstructure of all the as-prepared four samples were characterized using a scanning electron microscope (Philips XL 30 and JEOL JSM-6700F Field Emission, 10 kV), a transmission electron microscopy (TEM), and a high-resolution TEM (JEOL-2100 F, 200 kV).

Electrochemical measurements

The electrochemical properties were examined with CR2032 coin cells assembled in a glove box (Mbraun, Inc.) filled with pure argon gas with concentrations of moisture and oxygen below 0.1 ppm. The working electrodes were fabricated by casting the slurry (80 wt% of active materials, 10 wt% of acetylene black, and 10 wt% of polyvinylidene fluoride (PVDF) binder in N-methyl-2-pyrrolidinone (NMP)) onto the Cu foil as current collector, and then dried in a vacuum oven at 120 °C for 24 h to remove the solvent. Lithium foil was employed as the counter electrode, Celgard 2300 as the separator, and 1 M

LiPF₆ in a mixture of ethylene carbonate (EC) and dimethyl carbonate (DEC) (v/v=1:1) as the electrolyte. The discharge/charge performances of the electrodes were evaluated at room temperature using a multichannel battery testing system (LAND CT2001A). The cyclic voltammetry (CV) tests were carried out on a CHI606E electrochemical workstation (CHI Instrument Company) with lithium foil as both the counter and reference electrode over the potential range of 0.005-3.0 V (vs. Li⁺/Li) at a scanning rate of 0.2 mV s⁻¹. The electrochemical impedance spectroscopy (EIS) investigation was implemented by a Princeton Applied Research PARSTAT 2273 advanced electrochemical system in the frequency range from 100 kHz to 0.1 Hz with an amplitude of 5 mV.

Results and discussion

Figure 1 illustrates the preparation processes of the MnO@C NPs, MnO@C/CNTs and MnO@C/RGO nanohybrids. In a typical procedure for the MnO@C NPs preparation, the Mn(oleate)₂ was used as the raw materials and heated at 750 °C in an inert N₂ atmosphere, resulting in the formation of MnO@C NPs due to the confinement effect of carbon layers *in situ* formed by thermal decomposition and carbonization of the oleate anions. For preparing the advanced MnO@C/CNTs and MnO@C/RGO nanohybrids, additional CNTs and RGO materials should be well dispersed into the precursor solution of Mn(oleate)₂ in n-hexane, respectively. In the following heat treatment processes, the formed MnO@C NPs will attach onto the surfaces of already existed CNTs (RGO) materials, which play the significant role as highly conductive and flexible 1D (2D) conductive nano-networks when charging/discharging.

The composition, crystalline structure and phase purity of all the samples were firstly detected by the X-ray diffraction (XRD). Figure 2a compares the XRD patterns of all the C-MnO, MnO@C, MnO@C/CNTs and MnO@C/RGO materials. In

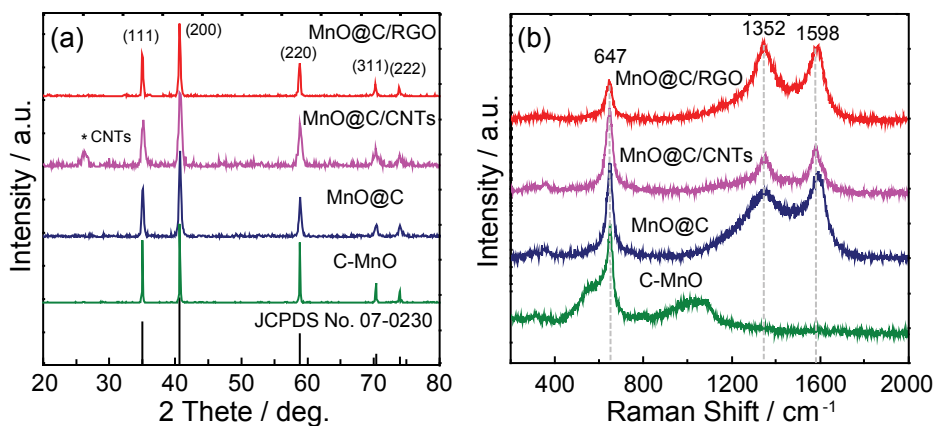


Figure 2. The comparisons of (a) XRD patterns and (b) Raman spectra between the C-MnO, MnO@C, MnO@C/CNTs and MnO@C/RGO nanohybrids.

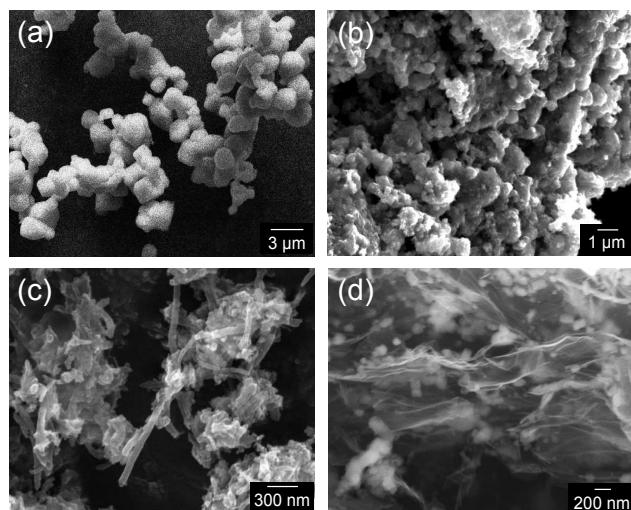


Figure 3. Typical SEM images of the (a) C-MnO, (b) MnO@C, (c) MnO@C/CNTs and (d) MnO@C/RGO nanohybrids.

addition to the weak diffraction peak at about 26.5° assigned to CNTs in the MnO@C/CNTs nanocomposites, all the intense peaks in the four spectra can be well indexed to a pure cubic phase of MnO materials [space group: Fm3m (225), JCPDS Card No. 07-0230] without any other impurities, indicating the high phase purity of all the MnO-based materials obtained. Furthermore, the peak widths at half maximum of the as-prepared materials are clearly wider than that of the commercial MnO, demonstrating their nanometer-sized nature instead of the micrometer size of C-MnO particles of $2\sim 3\ \mu\text{m}$ [as the scanning electron microscopy (SEM) image shown in Figure 3a]. The MnO crystallite size in the three prepared samples is ca. 100 nm by Scherrer's formula based on the widths of the major diffraction peaks of (200) and (111), which is well consistent with transmission electron microscopy (TEM) and SEM observations (Figures 3 and 4). Raman spectroscopy was further employed to characterize the structure and composition of all the MnO-based materials. As shown in Figure 2b, the Raman shift at about $647\ \text{cm}^{-1}$ can be ascribed to the vibration of Mn-O bonds,^{34, 51} confirming the existence of MnO materials in all samples. There also exist two broad peaks at 1352 and $1598\ \text{cm}^{-1}$, attributable to the D and G bands of carbonaceous materials respectively,^{28, 51} except for the C-MnO sample, one pure MnO material without the content of any carbonaceous materials.

The morphology and particle size of all the MnO-based materials were further investigated by SEM, TEM and high-resolution TEM (HRTEM) technologies. Figure 3 compares the typical SEM images between the C-MnO, MnO@C, MnO@C/CNTs and MnO@C/RGO nanohybrids. As shown in Figure 3a, the commercial MnO product is mainly composed of the 2-3 μm MnO microparticles with highly smooth surface. In the MnO@C materials, the sizes of carbon-coated MnO particles are significantly reduced because of the confinement effect of *in situ* formed carbon layers, and furthermore the

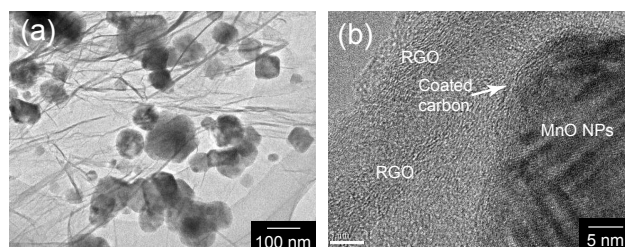


Figure 4. Typical (a) TEM and (b) HRTEM images of the MnO@C/RGO nanohybrids.

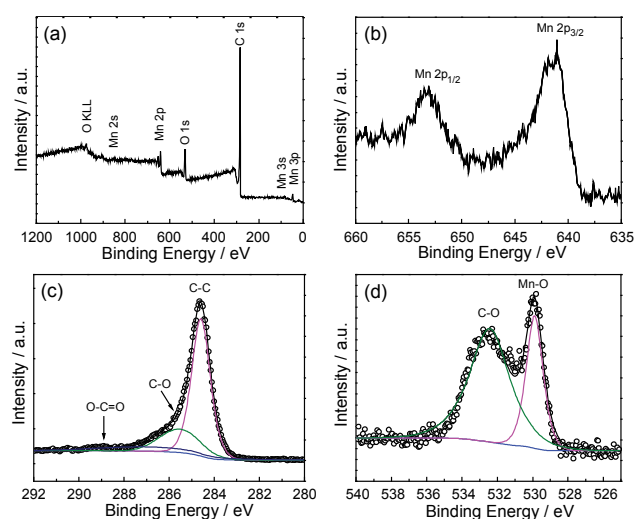


Figure 5. XPS spectra of the MnO@C/RGO nanohybrids prepared: (a) the survey spectrum and high-resolution spectra for (b) Mn 2p, (c) C 1s and (d) O 1s peaks.

surfaces of MnO@C NPs become rough originating from the coated carbon (Figure 3b). When the CNTs are introduced into the reaction system, the MnO@C NPs would attach upon the surfaces of CNTs, forming the MnO@C/CNTs nanocomposites (Figure 3c). Similarly, the MnO@C NPs can also adhere on both sides of RGO nanosheets and finally be wrapped into the interlayers of the formed 3D RGO network, resulting in the formation of MnO@C/RGO nanohybrids (Figure 3d). As described above, the highly conductive networks composed of the introduced 1D CNTs and 2D RGO materials will work as the electrical wires to conduct electrons upon cycling. Thus, it is rationally deduced that both of the as-prepared MnO@C/CNTs and MnO@C/RGO nanohybrids can exhibit much improved electrochemical properties compared to the C-MnO and MnO@C NPs ones when used as anode for LIBs, which will be confirmed in the following electrochemical tests. Figure 4 further shows the TEM and HRTEM images of MnO@C/RGO nanohybrids. It is clearly observed that, the MnO@C NPs of about 80-120 nm are tightly wrapped in the RGO networks. It is noteworthy that, the prepared MnO@C/RGO nanohybrids are extremely robust without the detachment of two constituents even after 6 h ultrasonication for preparing the TEM tests. In comparison, the MnO@C NPs can be stripped readily from the surfaces of CNTs, which may be one of the

main reasons for the reduced electrochemical properties of MnO@C/CNTs nanocomposites compared to the MnO@C/RGO one as demonstrated in the following section.

The X-ray photoelectron spectroscopy (XPS) measurements were further implemented to explore the elemental composition and surface electronic state of the MnO@C/RGO nanohybrids. As the survey XPS spectrum is shown in Figure 5a, the highest peak labeled as C1s should originate from the carbonaceous materials of RGO nanosheets and coated carbon on the surfaces of MnO NPs. It shows an asymmetrical profile owing to the presence of different oxygen containing groups covalently linked to the carbon atoms, and can be deconvoluted into three parts, including the peaks located at 284.6, 285.6 and 288.9 eV corresponding to C-C, C-O and O-C=O bonds respectively (Figure 5c).^{35, 52} In addition to the signal of carbon atoms, the survey XPS spectrum also reveals the existence of Mn and O elements. The peaks arising from the Mn (2s, 2p, 3s and 3p) and O (1s) can be assigned to the existence of MnO materials, which is in good accordance with the XRD and Raman test results. In the Mn2p high-resolution XPS spectrum (Figure 5b), two peaks at 641.1 and 653.1 eV can be clearly distinguished as the signals of Mn 2p_{3/2} and Mn 2p_{1/2}, agreeing well with the MnO materials reported in the previous literatures.^{28, 29} Furthermore, the O1s high-resolution XPS spectrum discloses two different states of oxygen atoms, i.e., manganese-oxygen (Mn-O) bonds at 529.9 eV (Mn-O) and carbon-oxygen (C-O, C=O and O-C=O) bonds at about 532.4 eV.^{29, 33}

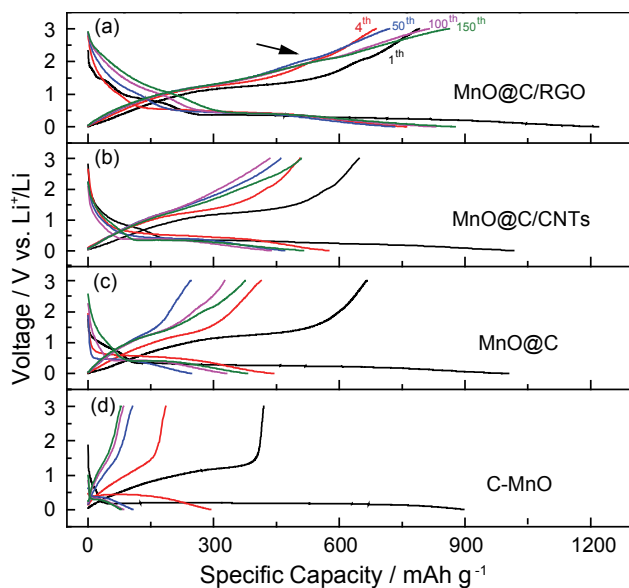


Figure 6. The galvanostatic discharge/charge profiles of (a) MnO@C/RGO, (b) MnO@C/CNTs, (c) MnO@C and (d) C-MnO materials. Note that, the fed current density of the 1st cycles is 0.08 A g⁻¹ while those of the other cycles are 0.38 A g⁻¹.

In order to demonstrate the structural and performance superiorities of MnO@C/RGO nanohybrids as anode materials for LIBs, its electrochemical properties were compared to the other three MnO-based materials of C-MnO, MnO@C NPs and MnO@C/CNTs nanocomposites. Figure 6 firstly compares the galvanostatic discharge/charge curves of the 1st, 4th, 50th, 100th and 150th cycles. Note that, all the cells were cycled at the current density of 0.38 A g⁻¹ after three low-current-density (0.08 A g⁻¹) cycles, i.e., the 1st curves are recorded at 0.08 A g⁻¹ while the other cycled at 0.38 A g⁻¹. It is clearly disclosed that the MnO@C/RGO nanohybrids exhibit the best electrochemical properties in terms of the highest specific capacity and optimal cycling stability compared to the other three samples. Specifically, (i) the specific reversible capacity (C_{sr}) of the 1st cycle for the MnO@C/RGO nanohybrids is ca. 791 mA h g⁻¹, which is obviously higher than 419, 665 and 646 mA h g⁻¹ for C-MnO, MnO@C NPs and MnO@C/CNTs nanocomposites respectively; (ii) in the cycling processes, the MnO@C/RGO nanohybrids exhibit more excellent maintenance of discharge/charge curves, including the shapes, potentials of the plateaus, polarizations between the charge and discharge plateaus and specific capacities, in comparison with the other three comparative materials; (iii) after 150 cycles, the C_{sr} value of MnO@C/RGO nanohybrids gradually increases to 862 mA h g⁻¹ from 687 mA h g⁻¹ of the 4th cycle, while those of C-MnO and MnO@C NPs contrarily decrease to 78 and 375 mA h g⁻¹ from 184 and 413 of the 4th cycles respectively, and that (509 mA h g⁻¹) of MnO@C/CNTs nanocomposites is almost equal to 506 mA h g⁻¹ of the 4th cycles with a minimum value at about the 150th cycle. Furthermore, there exists one additional plateau (denoted by the arrow in Figure 6a) at about 2.07 V vs. Li⁺/Li in the delithiation curves of the MnO@C/RGO nanohybrids, which is obviously different from the absences of such plateaus for the other comparative materials. According to the previously reported papers,^{30, 33} this high-voltage charge plateau should be ascribed to the oxidation reaction of Mn²⁺ to Mn⁴⁺. Those may be originated from the existence of superior carbon conductive networks in MnO@C/RGO nanohybrids, because they can efficiently promote the kinetics of electrochemical reactions and hence enable the conversion of Mn²⁺ to Mn⁴⁺ at the relatively low potential of about 2.07 V vs. Li⁺/Li, which is unlikely to be achieved in the other comparative materials due to the absence of such advanced conductive networks.

High-rate performance is one of the most important electrochemical properties of LIBs for high-power applications. Hence, the lithium-storage rate capabilities of all the four materials are further evaluated and compared at variable current densities from 0.08 to 7.6 A g⁻¹ (Figure 7a). The results clearly show that MnO@C/RGO nanohybrids exhibit the best

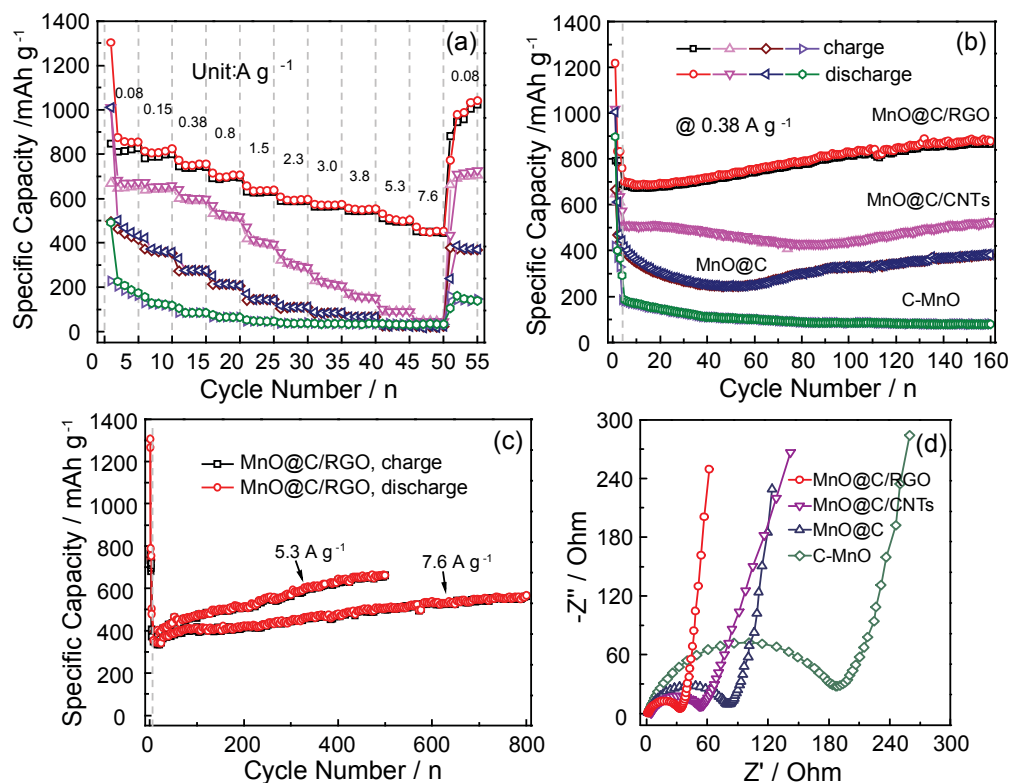


Figure 7. The comparisons of (a) rate capabilities, (b) cycling performances and (d) EIS spectra between the C-MnO, MnO@C NPs, MnO@C/CNTs nanocomposites and MnO@C/RGO nanohybrids. The fed current density for cycling tests is 0.38 A g^{-1} after the first three cycles at a relatively low current density of 0.08 A g^{-1} . (c) The high-rate cycling performances of MnO@C/RGO nanohybrids after three low-rate cycles at 0.08 A g^{-1} .

high-rate performance as well as highest specific capacities among them. For example, the reversible capacity of MnO@C/RGO nanohybrids at a moderate current density of 0.38 A g^{-1} (corresponding to a theoretical rate of 0.5C, i.e., completing the charging or discharging process within 2 hours) is about 741.4 mAh g^{-1} , which is significantly higher than 593.6 , 274.2 and 84.7 mAh g^{-1} of the MnO@C/CNTs, MnO@C NPs and C-MnO materials respectively. At a very high current density of 7.6 A g^{-1} , the MnO@C/RGO nanohybrids can still deliver a specific capacity of 448.2 mAh g^{-1} , even higher than 372 mAh g^{-1} of the theoretical capacity of graphite materials, while such a high current density incapacitates the other three MnO-based materials for lithium storage.

Moreover, the cycling performances of MnO@C/RGO nanohybrids are also greatly superior to those of the others, promising it a long-life anode material for LIBs. As shown in Figure 7b, the retained reversible capacity of the MnO@C/RGO nanohybrid is up to 863 mA h g^{-1} after 160 cycles at the current density of 0.38 A g^{-1} , while those of C-MnO, MnO@C NPs and MnO@C/CNTs nanocomposites are only 85 , 274 and 593 mA h g^{-1} respectively after the same cycles. More importantly, the MnO@C/RGO nanohybrid can still achieve excellent lithium-storage cycles at very high current densities with slight capacity increase rather than fading (Figures 7b and c). Taking the current density of up to 7.6 A g^{-1} as the example, the

lithium-storage capacity remains 562 mA h g^{-1} after 800 cycles with a capacity increase rate of 0.064% per cycle. Additionally, the MnO NPs in the MnO@C/RGO nanohybrid can still keep its original morphology and size even after 100 cycles at a very high current density of 7.6 A g^{-1} , which is disclosed in Figure S1 in the Supporting Information.

In addition to the result that MnO@C/RGO nanohybrid exhibit the best electrochemical properties, it can also be readily concluded that, the superiority sequence is MnO@C/RGO > MnO@C/CNTs >> MnO@C NPs > C-MnO when used as anode materials for LIBs. In comparison with C-MnO, the ordinary MnO@C NPs exhibit improved electrochemical properties in terms of higher lithium-storage capacity (450 vs. 190 mA h g^{-1} at a low current density of 0.08 A g^{-1}), increased rate capabilities under the current densities of 2.3 A g^{-1} and cycling capacities (for example, 380.8 vs. 79.3 mA h g^{-1} after 160 cycles at 0.38 A g^{-1}), which may be attributed to their nanoscale particle size and coated carbon layer on them as disclosed above. While the former can shorten the Li transport path and hence increase the percentage of active MnO materials, the latter is very efficient to promote the conductivity and stabilize the surfaces. Furthermore, the electrochemical properties of MnO@C NPs can be further improved to a higher level, when the second carbonaceous phase (CNTs or RGO) are added. For example, the CNTs can

promote the specific capacity of MnO@C NPs to about $653.3 \text{ mA h g}^{-1}$ by forming the MnO@C/CNTs nanocomposites, in which the CNTs act as the highly conductive wires connecting all the MnO@C nanoparticles. However, the enhancements of high-rate capabilities are limited by the CNTs employment (Figure 7a). Very interestingly and significantly, 2D RGO nanosheets play a more pronounced role in the improvements of rate performances as well as specific capacity in comparison with the 1D CNTs additives. After the RGO materials instead of CNTs are employed, the very high rate capabilities can be significantly achieved as already discussed above, while the specific capacity further increases up to $823.5 \text{ mA h g}^{-1}$.

In order to further understand the differences of electrode reaction kinetics, Figure 7d compares the EIS patterns of all four materials. As disclosed, all the Nyquist plots exhibit the similar profiles, consisting of a depressed semicircle followed by an inclined line in the low frequency range. The intercept on the Z_{re} axis at the high frequency corresponds to the combined resistance of the electrolyte and electrode (R_e), the semicircle in the high-medium frequency region is attributed to the charge-transfer impedance (R_{ct}) at the electrode-electrolyte interface, and the inclined line in the low frequency range is assigned to the lithium diffusion process or so-called Warburg diffusion. Although the R_e values of all four samples are almost the same, the R_{ct} of C-MnO electrode is obviously larger than the other three, demonstrating that the carbon modification and nanocrystallization can effectively facilitate the processes of charge transfer. In comparison with the MnO@C sample, the MnO@C/CNTs material exhibits the relatively smaller R_e value, which may be due to the higher conductivity of the additive 1D CNTs than the coated carbon layers on the MnO nanoparticles. As expected, the MnO@C/RGO exhibits the smallest R_e value amongst all the samples due to high electron quality and unique 2D nanostructure. Those indicate that, the flexible 2D nanostructure composed of RGO materials should be more effective in MnO-based nanohybrids materials to construct the conductive networks.

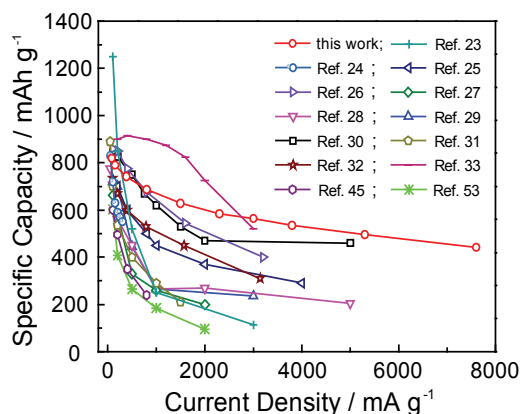


Figure 8. The comparison of rate capabilities of the MnO based composites between the present work and previously reported ones.

Additionally, we have also compared the electrochemical properties of our MnO@C/RGO nanohybrids with those of previously reported MnO based materials^{23-33, 45, 53}. As the comparison results shown in Figure 8, the present MnO@C/RGO nanohybrid exhibits much improved electrochemical properties, particularly high-rate capabilities, compared with most of the reported ones, which should be attributed to its novel nanostructures, including nanometer-sized MnO particles, uniform surface coating of carbon layers and the flexible 3D conductive networks

composed of 2D graphene materials. Firstly, the very small MnO particulates can provide shorter lithium transport distance and time compared with micrometer ones. Secondly, the coated carbon on the surfaces of nano-MnO particles can effectively stabilize the interphase between electrode and electrolyte. Thirdly, the flexible 3D conductive networks may be more beneficial for the improvements of electrochemical properties, because the graphene material could not only significantly reduce the dissolution and aggregation of MnO NPs during lithiation/delithiation process due to the wrapping

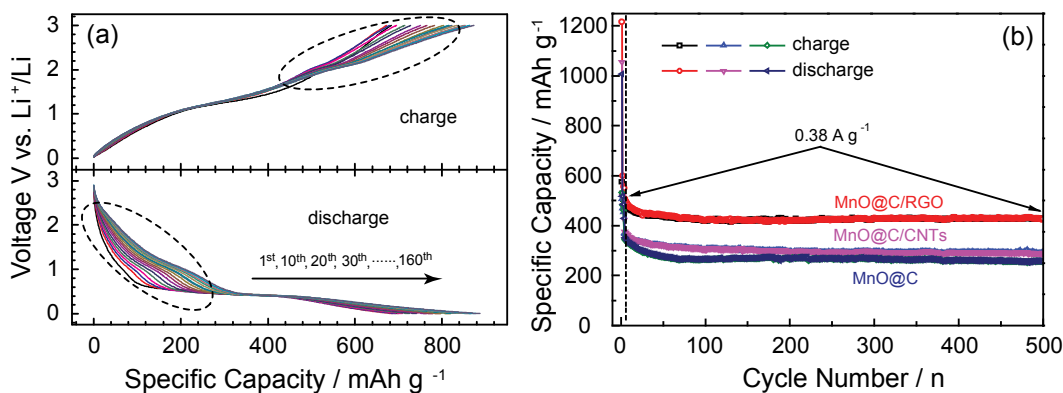


Figure 9. (a) The charge (upper) and discharge (lower) curves at the current density of 0.38 A g^{-1} after the first three cycles at 0.08 A g^{-1} . (b) The comparison of cycling performance cycled in the voltage range of $0.005\text{-}2.0 \text{ V vs. Li}^+/\text{Li}$.

effect of cloth-like graphene layers but also relieve the stress caused by the volumetric change during cycling owing to the elastic feature of flexible 2D graphene.

Nevertheless, there also exists one drawback to the MnO@C/RGO material when used as anode for LIBs, although it exhibits the optimal electrochemical properties compared with the others. As shown in Figures 7b and c, its specific capacities are progressively increasing along with cycle in the constant current charge/discharge process. Although this phenomenon should be a commonplace for the MnO based materials as many previous papers disclosed,^{33, 34, 37, 47, 48, 54} it is still hoped that the specific capacities of electrode materials can remain unchanged during cycling, because the gradual increase of reversible capacities not only is superfluous for practical application but also implies the existence of some electrochemical instabilities during cycling. In this paper, we further achieve this expectation through carefully analyzing the galvanostatic curves and then regulating the cut-off voltage ranges. As the charge and discharge curves disclosed in Figure 9a, it is interestingly found that there exists an obvious electrochemical activation above 2.0 V vs. Li⁺/Li, which should be the main reason of capacity increase during cycling. This activation process is also confirmed by the cyclic voltammetry (CV) profiles (not shown here). As one typical oxide anode material for LIBs, the MnO can reversibly store lithium in the low voltage range below 2.0 V based on the conversion reaction between Mn²⁺ and Mn⁰ species ($\text{MnO} + 2\text{Li}^+ + 2\text{e}^- \leftrightarrow \text{Mn} + \text{Li}_2\text{O}$), which corresponds to the plateaus of about 0.2 and 1.1 V in the discharge and charge curves of Figure 9a respectively. When further charged to higher voltage of above 2.0 V, the redox reaction of the Mn⁴⁺/Mn²⁺ couple will be activated, which had been demonstrated by Huang and co-workers through *ex-situ* XPS technologies³³. Thus, it could be rationally deduce that, the phenomenon of capacity increase with cycling would disappear, which had been firstly verified by reducing the cut-off voltage of cells. For example, the specific capacities keep almost constant when the cells galvanostatically cycled between 0.005 and 2.0 V vs. Li⁺/Li even after 500 cycles (as shown in Figure 9b). Therefore, the cycling performances of LIBs including half and full cells can be significantly improved by adjusting the test voltage range, which is still studying in our laboratory and will be published in future. In addition to the redox reaction of the Mn⁴⁺/Mn²⁺ couple, the carbonaceous materials existed in the nanohybrid should be also responsible for the phenomenon of capacity increase, which has been verified in our lab and will be further discussed in elsewhere.

Conclusions

In summary, one superior MnO based anode material for LIBs have been successfully prepared by rationally engineering the electronically conductive network and controlling the sizes and surfaces of MnO particulates. In the obtained nanohybrid, the

nanoscale MnO particles can effectively shorten the Li transport path and hence time, coated carbon layers on the surface of MnO nanoparticles are very efficient to promote the conductivity and stabilize the interfaces, and 3D networks composed of flexible 2D RGO nanosheets play a more pronounced role in the improvements of electrochemical properties due to its novel structure. Therefore, the MnO@C/RGO nanohybrid exhibits much improved electrochemical properties in terms of higher specific capacity, superior rate performances and excellent cycle life, in comparison with not only the commercial MnO material, MnO@C NPs and carbon nanotubes enhanced MnO@C/CNTs but also most of the previously reported MnO-based materials. Furthermore, we have also firstly improved its drawback of progressively increasing capacities as cycling by adjusting the voltage range after ascertaining the reasons. The structural design presented in this study not only represents a promising avenue for developing a superior MnO based materials with high-rate and long cycle life performances but also can be easily extended to the fabrication of other oxide anode materials for next-generation advanced LIBs.

Acknowledgements

This work was supported by the Fundamental Research Funds for the Central Universities (14QNJJ014), the Science Technology Program of Jilin Province (20140101087JC, 20150520027JH), Singapore MOE AcRF Tier 1 grants RG2/13, Singapore National Research Foundation under CREATE program: EMobility in Megacities, the National High Technology Research and Development Program of China (2013AA110103), New Century Excellent Talents Supporting Plan of Education Ministry (NCET-12-0816), Research and development of low temperature lithium iron phosphate power battery (Industry and Information Department of Jilin Province [2013] 323). XL thanks the support of the International Postdoctoral Exchange Fellowship Program.

Notes and references

1. B. Dunn, H. Kamath and J. M. Tarascon, *Science*, 2011, **334**, 928-935.
2. B. Kang and G. Ceder, *Nature*, 2009, **458**, 190-193.
3. Q. Zhang, E. Uchaker, S. L. Candelaria and G. Cao, *Chem. Soc. Rev.*, 2013, **42**, 3127-3171.
4. B. C. Melot and J. M. Tarascon, *Acc. Chem. Res.*, 2013, **46**, 1226-1238.
5. M. S. Whittingham, *Chem. Rev.*, 2014, **114**, 11414-11443.
6. J. B. Goodenough, *Acc. Chem. Res.*, 2013, **46**, 1053-1061.
7. D. W. Feng, C. Wang, W. T. Cheng, G. B. Li, S. J. Tian, F. H. Liao, M. Xiong and J. H. Lin, *Solid State Sciences*, 2009, **11**, 845-851.
8. X.-L. Wu, Y.-G. Guo and L.-J. Wan, *Chem-Asian J.*, 2013, **8**, 1948-1958.
9. M. N. Obrovac and V. L. Chevrier, *Chem. Rev.*, 2014, **114**, 11444-11502.

10. K. Amine, R. Kanno and Y. Tzeng, *MRS Bull.*, 2014, **39**, 395-401.
11. J. Maier, *Angew. Chem. Int. Ed.*, 2013, **52**, 4998-5026.
12. Z. Y. Wang, D. Y. Luan, S. Madhavi, Y. Hu and X. W. Lou, *Energy Environ. Sci.*, 2012, **5**, 5252-5256.
13. B. Wang, J. S. Chen, H. B. Wu, Z. Y. Wang and X. W. Lou, *J. Am. Chem. Soc.*, 2011, **133**, 17146-17148.
14. X. J. Zhu, Y. W. Zhu, S. Murali, M. D. Stoller and R. S. Ruoff, *ACS Nano*, 2011, **5**, 3333-3338.
15. X.-L. Wu, Y.-G. Guo, L.-J. Wan and C.-W. Hu, *J. Phys. Chem. C*, 2008, **112**, 16824-16829.
16. W.-M. Zhang, X.-L. Wu, J.-S. Hu, Y.-G. Guo and L.-J. Wan, *Adv. Funct. Mater.*, 2008, **18**, 3941-3946.
17. P. L. Taberna, S. Mitra, P. Poizot, P. Simon and J. M. Tarascon, *Nat. Mater.*, 2006, **5**, 567-573.
18. E. Kang, Y. S. Jung, A. S. Cavanagh, G.-H. Kim, S. M. George, A. C. Dillon, J. K. Kim and J. Lee, *Adv. Funct. Mater.*, 2011, **21**, 2430-2438.
19. G. M. Zhou, D. W. Wang, F. Li, L. L. Zhang, N. Li, Z. S. Wu, L. Wen, G. Q. Lu and H. M. Cheng, *Chem. Mater.*, 2010, **22**, 5306-5313.
20. X. Wang, X.-L. Wu, Y.-G. Guo, Y. Zhong, X. Cao, Y. Ma and J. Yao, *Adv. Funct. Mater.*, 2010, **20**, 1680-1686.
21. X. W. Lou, D. Deng, J. Y. Lee, J. Feng and L. A. Archer, *Adv. Mater.*, 2008, **20**, 258-262.
22. Z. S. Wu, W. C. Ren, L. Wen, L. B. Gao, J. P. Zhao, Z. P. Chen, G. M. Zhou, F. Li and H. M. Cheng, *ACS Nano*, 2010, **4**, 3187-3194.
23. H. T. Tan, X. H. Rui, Z. Y. Lu, C. Xu, W. L. Liu, H. H. Hng and Q. Y. Yan, *J. Phys. Chem. C*, 2014, **118**, 17452-17460.
24. X. Zhang, Z. Xing, L. L. Wang, Y. C. Zhu, Q. W. Li, J. W. Liang, Y. Yu, T. Huang, K. B. Tang, Y. T. Qian and X. Y. Shen, *J. Mater. Chem.*, 2012, **22**, 17864-17869.
25. T. Qiu, J. Wang, Y. L. Lu and W. S. Yang, *RSC Adv.*, 2014, **4**, 23027-23035.
26. K. Su, C. Wang, H. G. Nie, Y. Guan, F. Liu and J. T. Chen, *J. Mater. Chem. A*, 2014, **2**, 10000-10006.
27. T. Kokubu, Y. Oaki, E. Hosono, H. S. Zhou and H. Imai, *Adv. Funct. Mater.*, 2011, **21**, 3673-3680.
28. K. J. Zhang, P. X. Han, L. Gu, L. X. Zhang, Z. H. Liu, Q. S. Kong, C. J. Zhang, S. M. Dong, Z. Y. Zhang, J. H. Yao, H. X. Xu, G. L. Cui and L. Q. Chen, *ACS Appl. Mater. Interfaces*, 2012, **4**, 658-664.
29. Y. Xia, Z. Xiao, X. Dou, H. Huang, X. H. Lu, R. J. Yan, Y. P. Gan, W. J. Zhu, J. P. Tu, W. K. Zhang and X. Y. Tao, *ACS Nano*, 2013, **7**, 7083-7092.
30. H. Jiang, Y. j. Hu, S. J. Guo, C. Y. Yan, P. S. Lee and C. Z. Li, *ACS Nano*, 2014, **8**, 6038-6046.
31. W. M. Chen, L. Qie, Y. Shen, Y. M. Sun, L. X. Yuan, X. L. Hu, W. X. Zhang and Y. H. Huang, *Nano Energy*, 2013, **2**, 412-418.
32. G. L. Xu, Y. F. Xu, H. Sun, F. Fu, X. M. Zheng, L. Huang, J. T. Li, S. H. Yang and S. G. Sun, *Chem. Commun.*, 2012, **48**, 8502-8504.
33. Y. M. Sun, X. Hu, W. Luo, F. F. Xia and Y. Huang, *Adv. Funct. Mater.*, 2013, **23**, 2436-2444.
34. Y. Xiao, X. Wang, W. Wang, D. Zhao and M. H. Cao, *ACS Appl. Mater. Interfaces*, 2014, **6**, 2051-2058.
35. B. Liu, X. L. Hu, H. H. Xu, W. Luo, Y. M. Sun and Y. H. Huang, *Sci. Rep.*, 2014, **4**, 4229.
36. T. Y. Wang, Z. Peng, Y. H. Wang, J. Tang and G. F. Zheng, *Sci. Rep.*, 2013, **3**, 2693.
37. S. B. Wang, Y. B. Ren, G. R. Liu, Y. L. Xing and S. C. Zhang, *Nanoscale*, 2014, **6**, 3508-3512.
38. S. J. Prabakar, Y. H. Hwang, E. G. Bae, S. Shim, D. Kim, M. S. Lah, K. S. Sohn and M. Pyo, *Adv. Mater.*, 2013, **25**, 3307-3312.
39. J. Lin, Z. W. Peng, C. S. Xiang, G. D. Ruan, Z. Yan, D. Natelson and J. M. Tour, *ACS Nano*, 2013, **7**, 6001-6006.
40. X. S. Zhou, L. J. Wan and Y. G. Guo, *Adv. Mater.*, 2013, **25**, 2152-2157.
41. L. Wang, D. Wang, Z. H. Dong, F. X. Zhang and J. Jin, *Nano letters*, 2013, **13**, 1711-1716.
42. H. Liu, G. X. Wang, J. Liu, S. Z. Qiao and H. Ahnc, *J. Mater. Chem.*, 2011, **21**, 3046-3052.
43. B. Wang, X.-L. Wu, C.-Y. Shu, Y.-G. Guo and C.-R. Wang, *J. Mater. Chem.*, 2010, **20**, 10661-10664.
44. T. Tao, A. M. Glushenkov, C. Zhang, H. Zhang, D. Zhou, Z. Guo, H. K. Liu, Q. Chen, H. Hu and Y. Chen, *J. Mater. Chem.*, 2011, **21**, 9350-9355.
45. S. M. Guo, G. X. Lu, S. Qiu, J. R. Liu, X. Z. Wang, C. Z. He, H. G. Wei, X. R. Yan and Z. H. Guo, *Nano Energy*, 2014, **9**, 41-49.
46. S. Xin, Y.-G. Guo and L.-J. Wan, *Accounts of Chemical Research*, 2012, **45**, 1759-1769.
47. S. B. Wang, Y. L. Xing, H. H. Xu and S. C. Zhang, *ACS Appl. Mater. Interfaces*, 2014, **6**, 12713-12718.
48. J. W. Qin, Q. Zhang, Z. Y. Cao, X. Li, C. W. Hu and B. Q. Wei, *Nano Energy*, 2013, **2**, 733-741.
49. W. S. Hummers and R. E. Offeman, *J. Am. Chem. Soc.*, 1958, **80**, 1339.
50. J. Park, K. An, Y. Hwang, J. G. Park, H. J. Noh, J. Y. Kim, J. H. Park, N. M. Hwang and T. Hyeon, *Nat. Mater.*, 2004, **3**, 891-895.
51. Y. J. Mai, D. Zhang, Y. Q. Qiao, C. D. Gu, X. L. Wang and J. P. Tu, *J. Power Sources*, 2012, **216**, 201-207.
52. M. Letourneau, M. Tremblay, L. Faucher, D. Rojas, P. Chevallier, Y. Gossuin, J. Lagueur and M. A. Fortin, *J. Phys. Chem. B*, 2012, **116**, 13228-13238.
53. Z. Cai, L. Xu, M. Yan, C. Han, L. He, K. M. Hercule, C. Niu, Z. Yuan, W. Xu, L. Qu, K. Zhao and L. Mai, *Nano letters*, 2015, **15**, 738-744.
54. X. W. Li, S. L. Xiong, J. F. Li, X. Liang, J. Z. Wang, J. Bai and Y. T. Qian, *Chem. Eur. J.*, 2013, **19**, 11310-11319.

Table of Contents (TOC)

